



TITLE:

Universal Multistream Radial Structures of Cold Dark Matter Halos

AUTHOR(S):

Enomoto, Yohsuke; Nishimichi, Takahiro; Taruya, Atsushi

CITATION:

Enomoto, Yohsuke ...[et al]. Universal Multistream Radial Structures of Cold Dark Matter Halos. *The Astrophysical Journal Letters* 2023, 950(2): L13.

ISSUE DATE:

2023-06-20

URL:



<http://hdl.handle.net/2433/286093>

RIGHT:

© 2023. The Author(s). Published by the American Astronomical Society; Original content from this work may be used under the terms of the Creative Commons Attribution 4.0 licence. Any further distribution of this work must maintain attribution to the author(s) and the title of the work, journal citation and DOI.



Universal Multistream Radial Structures of Cold Dark Matter Halos

 Yohsuke Enomoto¹, Takahiro Nishimichi^{2,3,4} , and Atsushi Taruya^{2,3} 
¹Department of Physics, Kyoto University Kyoto 606-8502, Japan

²Center for Gravitational Physics and Quantum Information, Yukawa Institute for Theoretical Physics, Kyoto University, Kyoto 606-8502, Japan

³Kavli Institute for the Physics and Mathematics of the Universe (WPI), The University of Tokyo Institutes for Advanced Study, The University of Tokyo, 5-1-5 Kashiwanoha, Kashiwa, Chiba 277-8583, Japan

⁴Department of Astrophysics and Atmospheric Sciences, Faculty of Science, Kyoto Sangyo University, Motoyama, Kamigamo, Kita-ku, Kyoto 603-8555, Japan

Received 2023 February 17; revised 2023 May 2; accepted 2023 May 23; published 2023 June 20

Abstract

Virialized halos of cold dark matter generically exhibit multistream structures of accreted dark matter within an outermost radial caustic known as the splashback radius. By tracking the particle trajectories that accrete onto the halos in cosmological N -body simulations, we count their number of apocenter passages (p) and use them to characterize the multistream structure of dark matter particles. We find that the radial density profile for each stream, classified by the number of apocenter passages, exhibits universal features and can be described by a double power-law function comprising shallow inner slopes and steep outer slopes of indices of -1 and -8 , respectively. Surprisingly, these properties hold over a wide range of halo masses. The double power-law feature is persistent when dividing the sample by concentration or accretion rate. The dependence of the characteristic scale and amplitude of the profile on p cannot be replicated by known self-similar solutions, requiring consideration of complexities such as the distribution of angular momentum or mergers.

Unified Astronomy Thesaurus concepts: [Galaxy dark matter halos \(1880\)](#); [Large-scale structure of the universe \(902\)](#)

1. Introduction

Since its first indication by Zwicky (Zwicky 1933, 1937), dark matter has long been thought to be an essential ingredient to explain the cosmic structure formation across a wide range of observations. One important consequence, supported by various observations, is that dark matter forms, at the macroscopic level, a smooth distribution with virtually null initial local velocity dispersion, referred to as cold dark matter (CDM; Peebles 1982; Blumenthal et al. 1984; Peebles 1984). According to a widely accepted scenario, a collapse of CDM occurs within a cosmic web, leading to the formation of self-gravitating bound objects called dark matter halos. The late-time evolution of such halos is driven by the continuous accretion of surrounding dark matter onto the halo center and successive mergers with other halos, resulting in the structure of CDM halos exhibiting several characteristic features. One prominent feature, found in cosmological N -body simulations, is the so-called Navarro–Frenk–White (NFW) profile, first suggested by Navarro et al. (1996, 1997), which has had a significant impact on observations as a testing ground for the CDM paradigm. Another striking feature is the power-law nature of the pseudo-phase-space density profile defined by $Q(r) \equiv \rho(r)/\sigma^3(r)$, with $\rho(r)$ and $\sigma(r)$ being, respectively, the radial density and velocity dispersion profile (Taylor & Navarro 2001; Ludlow et al. 2010; Navarro et al. 2010). The slope found in simulations closely matches the prediction of the Bertschinger’s secondary infall model (Bertschinger 1985), indicating that the structure of halos is built up in a self-similar manner. These properties imply that there is something more fundamental underlying them, which could aid in understanding the origin of universalities.

In this Letter, we present an alternative way to characterize halo density profiles based on phase-space information. It is worth noting that the formation of CDM halos is accompanied by a shell crossing at an early phase of matter accretion, followed by a multistream motion of matter distribution. The multistream nature of halos has garnered recent attention, highlighted with a renewed interest as the outer boundary of the multistream region serves as a natural boundary of halos and is clearly demarcated by a radial caustic, manifested as a local steepening of the density profile, referred to as the splashback radius (e.g., Adhikari et al. 2014; Diemer & Kravtsov 2014; More et al. 2015). Motivated by these findings, Sugiura et al. (2020) developed a method using an extension of the SPARTA algorithm in Diemer (2017) to reveal the multistream nature of halos at the outer regions, and they found that about 30% of halos are well described by the self-similar solution of Fillmore & Goldreich (1984). In this Letter, by substantially refining their analysis based on high-resolution simulations with finely sampled snapshots out to an early halo formation, we are able to unveil the innermost parts of the multistream region, where we find that halos exhibit a universal feature in each multistream distribution.

2. Method

We analyze cosmological N -body simulations performed in a flat Λ CDM cosmology, which is consistent with recent observations of cosmic microwave background radiation (Planck Collaboration et al. 2016). We mainly analyze the simulation that follows the movements of 500^3 particles in a comoving box with a side length of $41 h^{-1}$ Mpc using the tree particle-mesh code GINKAKU (T. Nishimichi et al. 2023, in preparation). We employ a softening length of $4.1 h^{-1}$ kpc, which we denote by r_{LR} in what follows. The snapshots of the particles are saved at 1001 redshifts, evenly spaced between $z = 0$ and 5, providing a dense sampling to accurately determine the number of apocenter

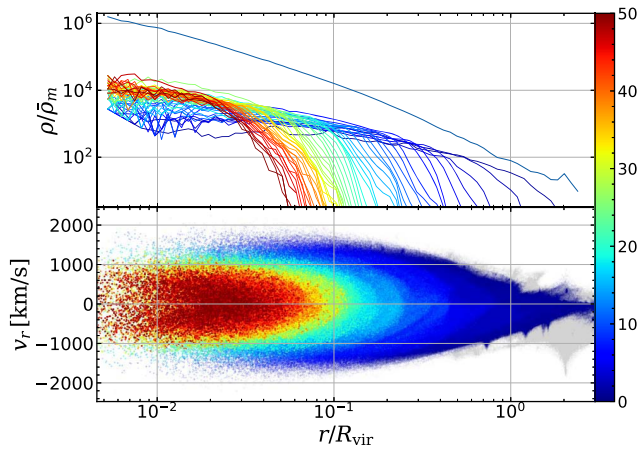


Figure 1. Radial density profile (upper) and phase-space distribution (lower) of a halo with $M_{\text{vir}} = 1.49 \times 10^{14} h^{-1} M_{\odot}$. The upper panel shows the decomposition of the total density profile (highest line) into the contributions from N -body particles with different numbers of apocenter passages, represented by colors ranging from $p = 1$ (dark blue) to $p = 50$ (dark red). The results are all normalized by the background matter density of the universe, $\bar{\rho}_m$. The lower panel displays the distribution of individual particles, with the same color-coding. The infalling component, $p = 0$, is depicted in gray.

passages (denoted by p in what follows) up to ~ 50 , following the method of Sugiura et al. (2020) with minor modifications.

We first select relaxed halos from those identified by ROCKSTAR (Behroozi et al. 2013) at $z = 0$ by imposing a cut in the spin parameter and the offset between the center of mass and the density peak (Klypin et al. 2016). We also discard subhalos according to the consistency between the exact spherical-overdensity mass and that listed in the ROCKSTAR catalog. We then trace the main progenitor by following the particles within the virial radius back in time, updating the center and the list of member particles using the shrinking-sphere method at each snapshot until we reach the first snapshot at $z = 5$ or when the number of member particles falls below 1000. Our final halo trajectories are defined as the center of mass of the 1000 fixed-member particles, which are closest in phase space to the center of the main progenitor at the highest redshift to which we can trace the progenitor with at least 1000 particles. We next follow forward in time the center of mass of these fixed particles to obtain a smooth trajectory robust to merger events. We monitor the velocities and positions of all surrounding particles that are within $2.5 R_{\text{vir}}$ at $z = 0$ relative to the center of the progenitor. We define and count the apocenter passage for each particle when the relative velocity changes from outgoing to infalling and the relative position has orbited at least 90° from the previous apocenter passage (Sugiura et al. 2020). These specific choices are found to be robust for the determination of the number of apocenter passages up to ~ 50 .

In Figure 1, we present the radial density profile and phase-space distribution of a representative halo with mass $M_{\text{vir}} = 1.49 \times 10^{14} h^{-1} M_{\odot}$, color-coded by the number of apocenter passages, p . It is apparent that particles with a high value of p tend to be concentrated at smaller radii, leading to an onion-like multistream structure in the phase-space distribution. We also confirmed that tangential velocity dispersion decreases with increasing p . On the other hand, the density profiles exhibit similar features, with the inner and outer slopes converging to a specific value regardless of p . In the

Table 1
Halo Samples in the LR Simulation

Sample	$10^{11} M_{\text{vir}} (h^{-1} M_{\odot})$	$R_{\text{vir}} (h^{-1} \text{Mpc})$	# of Halos
S	[3.16, 5.71]	[0.14, 0.17]	300
M	[5.71, 24.2]	[0.17, 0.27]	300
L	[24.2, 134]	[0.27, 0.48]	70
XL	[134, 1530]	[0.48, 1.08]	13

Note. The second, third, and fourth columns, respectively, show the range of halo masses, virial radii, and the number of halos.

following sections, we will further analyze this behavior for halos with different properties.

In order to study the convergence, we have conducted a higher-resolution simulation with 2000^3 particles with an identical initial Gaussian random field. However, storing as many as $\gtrsim 1000$ snapshots from this simulation requires a significant amount of disk space, and an accurate apocenter count would be costly. Therefore, we only use this run to verify the density profile at $z = 0$. In the following discussion, we refer to this simulation as HR, while the one with 500^3 particles is called LR. The softening scale for HR is $r_{\text{HR}} = 1.025 h^{-1} \text{kpc}$.

3. Results

In order to systematically and quantitatively investigate the radial density profile of particles with p apocenter passages, we divide the halos into four mass bins (Table 1). For each mass bin, we measure the stacked profile for each stream by rescaling the radial coordinate by the virial radius and the density by the virial mass for individual halos. We find that the stacked profile for each p , as presented in the upper panels and the lower left panel in Figure 2, are well fitted by the following functional form⁵:

$$\rho_{\text{stream}}(r; p) = \frac{A(p)}{\{r/S(p)\}[1 + \{r/S(p)\}^{\beta}]}, \quad (1)$$

where the characteristic scale $S(p)$ and density $A(p)$ are given as a function of p . Due to the rescaling in the stacking, the functions, $S(p)$ and $A(p)$, are quite similar among the four mass bins, as shown in Figure 3. We find that these functions are well captured by

$$\log_{10}\{A_{\text{fit}}(p)/\bar{\rho}_m\} = 4.89 - 0.119 \log_{10}(M_{\text{vir},10}) + \{-3.89 + 0.243 \log_{10}(M_{\text{vir},10})\} p^{-9/40}, \quad (2)$$

$$\log_{10}\{S_{\text{fit}}(p)/R_{\text{vir}}\} = 2.46 - 0.0474 \log_{10}(M_{\text{vir},10}) + \{-2.29 - 0.0639 \log_{10}(M_{\text{vir},10})\} p^{1/8}, \quad (3)$$

including the weak mass dependence, where $M_{\text{vir},10}$ is defined by $M_{\text{vir}}/10^{10} h^{-1} M_{\odot}$.

In Figure 2, the stacked profiles are presented up to $p = 40$. The horizontal axis is scaled by (p/R_{vir}) and the vertical axis by $(10^{p/4} r/\bar{\rho}_m)$ for improved visibility. The error bars indicate the standard error of the stacked profiles. The profiles are in agreement with Equation (1) over a wide range of radii and mass scales. A sharp cutoff is observed in the profile at large radii, which is consistent with our model with the asymptotic slope of

⁵ The fitting analysis employs the standard χ^2 method, with weights determined by the inverse variance among the stacked halos. Radial bins with $r > 1.2 r_{\text{LR}}$ are considered.

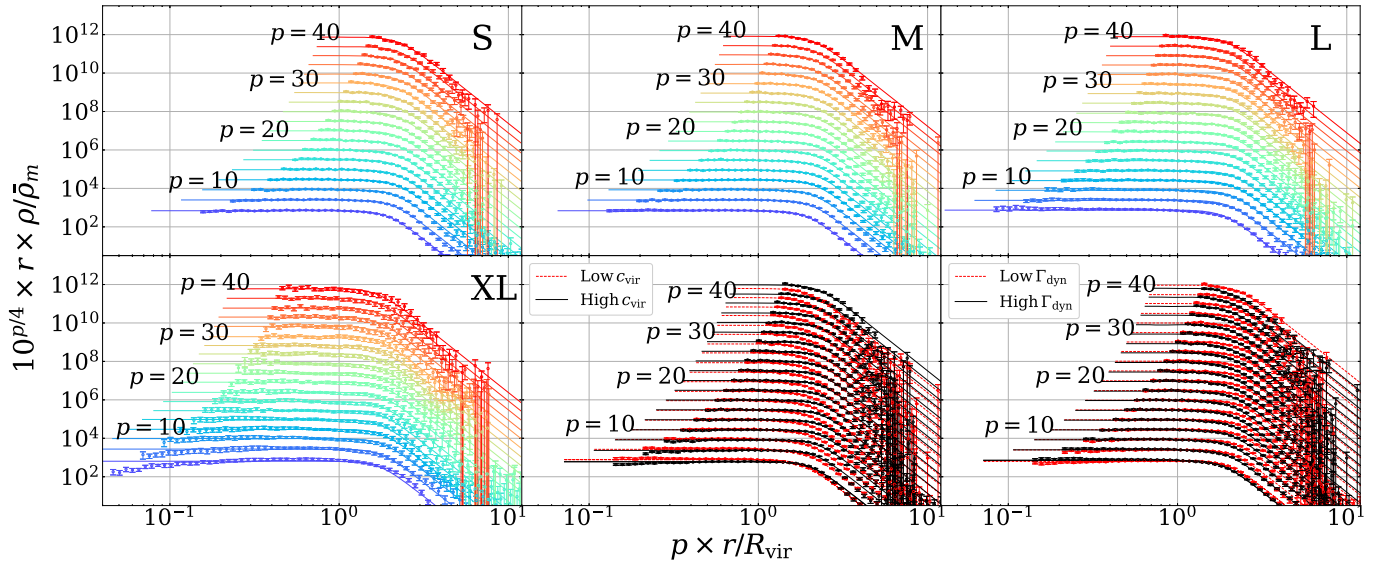


Figure 2. Stacked radial density profiles of N -body particles with even number of apocenter passages, ranging from $p = 4$ to 40. The four mass bins are displayed in the upper three and the lower left panel for S, M, L, and XL, respectively. Additionally, the lower middle and right panels show the results obtained from 460 halos in the mass range $[4.10^{11}, 2.30 \times 10^{12}] h^{-1} M_{\odot}$, which are further divided into the two subsamples based on the concentration parameter c_{vir} and accretion rate Γ_{dyn} , respectively (see Section 4.1 in detail). In each panel, the fitted results with Equation (1) are depicted as solid lines.

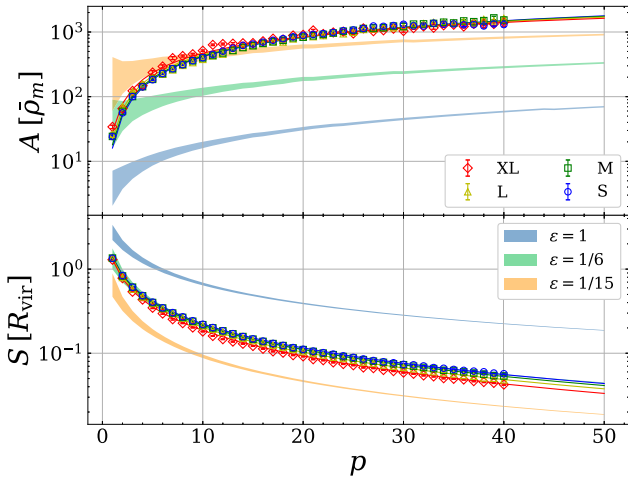


Figure 3. Dependence of the characteristic density A (upper) and scale S (lower) on the number of apocenter passages, p , as determined by fitting to Equation (1) for each mass bin (see legend). The thin solid curves represent the fitting formulae, Equations (2) and (3). For comparison, predictions of the Fillmore–Goldreich self-similar solutions are also shown for specific values of the parameter ϵ (1/15, 1/6 and 1). In plotting these predictions, we identify the position of radial caustics in the self-similar solutions with the characteristic scale $S(p)$ and derive $A(p)$ by equating the masses contained in each stream. The shaded regions for the predictions indicate uncertainty in identifying $S(p)$ with the position of the p th or $(p + 1)$ th radial caustics of the self-similar solutions.

–8 (see also Diemer 2023 for an alternative characterization of the outer cutoff for orbiting particles). More notably, the inner slope tends to be consistent with -1 for most cases, except for orbits with $p \lesssim 10$ for the XL sample, which exhibit a shallower slope. This is likely due to the sensitivity of these low- p orbits to recent mass accretion or merger history (e.g., Sugiura et al. 2020). However, this trend tends to be erased after several orbits, reaching a universal slope for $p \gtrsim 10$, indicating a self-similar growth of phase-space structure.

To quantitatively assess the double power-law nature of each stream, we compare the total density profile from HR for halos that have been matched with LR to the prediction obtained by

summing the individual double power-law profiles described by Equations (1)–(3).⁶ The results are shown in Figure 4, where the solid lines with shaded regions represent the prediction based on the double power-law model, taking into account the uncertainties in the numerical coefficients in the fit. Our model is in good agreement with HR for all four mass bins. Notably, we can recover the profile even at $r/R_{\text{vir}} \leq 1.2 \text{Max}(r_{\text{LR}}/R_{\text{vir}})$, despite the fact that the individual profiles for each p are fitted to the scales larger than $1.2 \text{Max}(r_{\text{LR}}/R_{\text{vir}})$ and only up to $p = 40$. This suggests that the model effectively extrapolates the mass distribution to large values of p beyond the resolution limit of LR. In the lower panel, we can observe the transition of the slope from -3 to -1 in different models.⁷

4. Discussion

4.1. Dependence on Halo Samples

The remarkable double power-law features in Section 3 are seen in mass-selected halo samples. Here, to assess the robustness of our findings, we analyze a subset of 460 halos within a specific mass range $[4.10 \times 10^{11}, 2.39 \times 10^{12}] h^{-1} M_{\odot}$. These halos are divided into two subsamples based on two different criteria. We employ the concentration parameter c_{vir} , defined by the ratio R_{vir}/R_s with R_s being the scale radius of the NFW profile and the mass accretion rate defined by $\Gamma_{\text{dyn}}(t) \equiv \{\log[M(t)] - \log[M(t - t_{\text{dyn}})]\} / \{\log[a(t)] - \log[a(t - t_{\text{dyn}})]\}$, with t_{dyn} being the dynamical time estimated from halo masses (Diemer 2017).⁸ Note that the radius R_s is estimated in rockstar based on the maximum circular velocity (Klypin et al. 2011). In both cases, we divide the halos into two halves, one with high values of these indicators and the other with low values.

⁶ In the plot, the summation is conservatively taken up to $p = 3000$. The change in density is less than 0.2% over the plotted range when we instead stop at $p = 300$.

⁷ The logarithmic slope is estimated from discrete simulation data points with statistical noise using the GEORGE Python package (Ambikasaran et al. 2015) for the Gaussian process.

⁸ We use the virial mass, M_{vir} , to measure Γ_{dyn} , whereas Diemer (2017) uses $M_{200\text{m}}$.

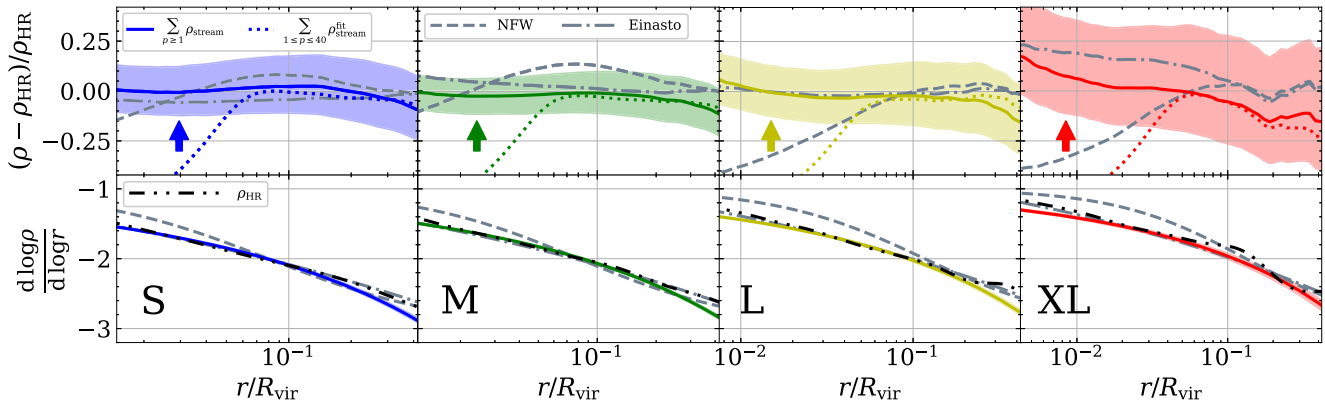


Figure 4. Comparison of the total density profile between our model ($\sum \rho_{\text{stream}}$) and HR (ρ_{HR}). The upper and lower panels, respectively, show the fractional difference with respect to HR, i.e., $(\rho - \rho_{\text{HR}})/\rho_{\text{HR}}$, and the logarithmic slope, $d \log \rho / d \log r$. The results for four mass bins are presented separately in each panel for scales above $2 \text{Max}(r_{\text{HR}}/R_{\text{vir}})$, i.e., twice the maximum value of the ratio $r_{\text{HR}}/R_{\text{vir}}$ estimated for individual halos in each mass bin. The shaded regions indicate the estimated uncertainties in the prediction, which are propagated from the statistical error in the stacked profile through the uncertainties in the fitting parameters. We also plot the NFW (dashed) and Einasto (dotted–dashed; Einasto 1965) profiles, obtained by fitting HR in the range $2 \text{Max}(r_{\text{HR}}/R_{\text{vir}}) \leq r/R_{\text{vir}} \leq 0.9$. In the upper panels, the results obtained from a partial summation of the double power-law profile up to $p = 40$ are also plotted (dotted). The vertical arrows indicate the scale of $1.2 \text{Max}(r_{\text{LR}}/R_{\text{vir}})$, corresponding to the convergence radius above which measured profiles from LR and HR simulations agree well with each other at $\sim 3\%$ precision.

The middle bottom (right bottom) panel of Figure 2 depicts the results for two subsamples having low and high values of c_{vir} (Γ_{dyn}), represented by red and black colors, respectively. Again, a good agreement between the double power-law function and measured profiles is observed over a wide range of p . A close look at each stream profile reveals that halos with a high concentration or low accretion rate tend to have a large amplitude $A(p)$ and a large characteristic scale $S(p)$. These trends are particularly evident for larger p , suggesting that the universal double power-law feature is established in a self-regulated manner during the orbital motion in the multistream region, where the diversity of mass accretion and merger histories tend to be erased and only be imprinted in $A(p)$ and $S(p)$.

4.2. Comparison with Self-similar Solutions

The results in Sections 3 and 4.1 strongly indicate that the inner structure of halos is built up dynamically in a self-similar manner. Here, we compare our results with self-similar solutions. While self-similar solutions are only valid in the Einstein–de Sitter universe, the secondary infall model of Bertschinger (1985) has been shown to reproduce the pseudo-phase-space density of $Q(r) \propto r^{-1.875}$ found in simulations in the Λ CDM model. Along the line of this, we consider the spherically symmetric solutions put forth by Fillmore & Goldreich (1984), which include Bertschinger’s secondary infall model as a special case. Recent work by Sugiura et al. (2020) has made a direct comparison of these predictions with radial multistream structures obtained from simulations up to $p = 5$. Identifying the position of radial caustics in self-similar solutions with the characteristic scale of the double power-law profile in Equation (1), it is possible to make predictions for both $A(p)$ and $S(p)$.

In Figure 3, we compare the predictions of self-similar solutions with our N -body results for three values of the model parameter ϵ , which describes the power-law slope of initial density contrast. Note that the parameter ϵ is restricted to the range $[0, 1]$, and the solution with $\epsilon = 1$ corresponds to Bertschinger’s secondary infall model. Figure 3 shows that none of the solutions consistently explain the trends in both $A(p)$ and

$S(p)$ although setting the parameter ϵ to $1/6$ reproduces the characteristic scale $S(p)$ reasonably well. The main reason for this failure is that for each stream, the Fillmore–Goldreich solutions predict a steep inner profile with a logarithmic slope of around -2 , irrespective of the value of ϵ . One possible explanation for the shallow inner cusps found in simulations is to introduce the nonzero angular momentum, which can reduce the steepness of the profile near the halo center (Nusser 2001; Zukin & Bertschinger 2010). However, existing solutions allow for the introduction of angular momentum in a very specific manner, and without a broad angular momentum distribution, they fail to describe the shallow inner cusp seen in the profile for each p .

We thus conclude that a more comprehensive theoretical study is needed to fully understand the universal features found in this Letter, taking into account the complexities associated with mass accretion and merger history. This may involve exploring the angular momentum distribution or relaxing the symmetry assumptions (see Ryden 1993; Lithwick & Dalal 2011 for the latter aspect).

4.3. On the Emergence of Double Power-law Nature

As a final discussion toward a better understanding of the origin of the universal double power-law nature, we focus on the halo sample M in Table 1 and select the particles with $p = 4, 10, 20,$ and 40 at $z = 0$. Then, we trace back their trajectories to higher redshifts and measure the density profiles for each value of p stacked over different halos. Figure 5 overplots the results at $z = 0.3$ (green) and 1.6 (red), on top of those at $z = 0$ already shown in Figure 2 (black). Clearly, the profiles vary over redshifts, and the amplitude of density gets increased with decreasing z . Interestingly, however, the evolution of the inner profiles becomes significantly weaker as the value of p increases, and at $p = 40$, the profiles almost converge even at the outermost part. This suggests that the double power-law nature was established at an early stage of the halo formation and remains stable against matter accretion, which can only affect the outer part of the density profile represented by particles with small values of p . Apart from the origin of the universal profiles, this picture is consistent with previous studies

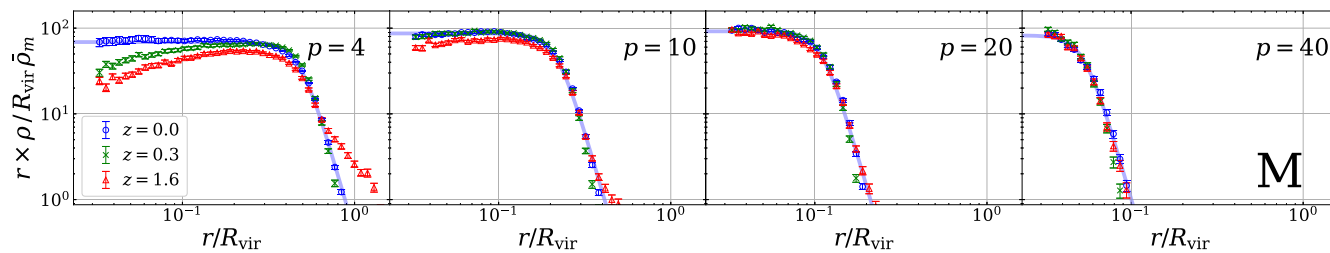


Figure 5. Stacked density profiles for the halo sample M measured at $z = 0$ (blue), 0.3 (green), and 1.6 (red). From left to right panels, results for the particles with $p = 4$, 10, 20, and 40 are respectively shown. Note that in each panel, the number of apocenter passages p is the one measured at $z = 0$, and we simply trace back the particles identified at $z = 0$ to higher redshifts $z = 0.3$ and 1.6. Each profile is computed in physical units (not comoving) and normalized by the virial radius R_{vir} (horizontal axis) and background mass density $\bar{\rho}_m$ (vertical axis) at $z = 0$. For ease of comparison, we also multiply the resultant density by r . The error bars indicate the standard error of the stacked profiles.

that show that the accreting matter mainly piles up at the outer region (e.g., Zhao et al. 2003) and partly explains why the characteristic scale $S(p)$ in Equation (1) is a decreasing function of p ; particles with large p have accreted earlier, and their distribution tends to be relaxed at the inner part of halos. In this respect, the dynamics at the early stage of halo formation would be the key to clarifying the origin of the double power-law nature.

5. Conclusion

In this Letter, we have investigated the multistream radial structures of dark matter halos in cosmological N -body simulations. Our focus is on the radial distribution of dark matter particles within the splashback radius. We use the method developed by Sugiura et al. (2020) to trace the trajectories of dark matter particles and quantify the density profile for each stream, which we label by p . With the help of 1001 snapshots between $z = 0$ and 5, we are able to resolve the multistream structure in phase space up to $p = 40$. The radial density profiles for each stream are accurately described by a double power-law function (Equation (1)), with characteristic density $A(p)$ and scale $S(p)$ well fitted, respectively, to Equations (2) and (3). These results are consistent across different sample selections based on the concentration parameter and mass accretion rate. We can recover the total density profile by summing up the individual contribution modeled by Equation (1), which provides a prediction comparable to or even better than the Einasto profile. Our findings suggest that the double power-law nature seen in the stream profiles is universal. This remarkable characteristic appears to have been established during an early stage of matter accretion and remains stable. To gain a deeper understanding of these results, we compare them with predictions based on self-similar solutions. We find that the Fillmore–Goldreich solutions (nor Bertschinger’s solution as a special case) cannot consistently explain both $A(p)$ and $S(p)$. This suggests that a more comprehensive theoretical study is necessary, taking into account the dynamical complexities associated with halo accretion and merging history.

The universal features of halos found in this Letter are a direct consequence of the cold nature of dark matter and serve as valuable insights into the physical properties of CDM halos. While this study has utilized N -body simulations and investigated the inner multistream structure up to $p = 40$, recent developments in simulating collisionless self-gravitating systems through Vlasov–Poisson equations offer a promising way to further probe the phase-space structure (Yoshikawa et al. 2013; Hahn & Angulo 2016; Sousbie & Colombi 2016). This

would provide a deeper understanding of the physics behind the universal features. To search for observational evidence of this universality, it would also be beneficial to investigate the impact of baryonic feedback through hydrodynamical simulations.

Finally, another point worth further investigating is to scrutinize the radial phase-space structures for alternative dark matter models as the nature of dark matter has a significant impact on small-scale structure formation (e.g., Bullock & Boylan-Kolchin 2017 for a review). Our method to reveal multistream structures can be straightforwardly applied to simulations of other dark matter models. Any difference in the radial multistream structures could provide valuable observational probes to clarify the nature of dark matter.

Acknowledgments

We thank Stéphane Colombi and Takashi Hiramatsu for insightful suggestions and discussions and Shogo Ishikawa and Satoshi Tanaka for comments and discussions. This work was supported in part by MEXT/JSPS KAKENHI grant Nos. JP19H00677 (TN), JP20H05861, JP21H01081 (AT and TN), and JP22K03634 (TN). We also acknowledge financial support from Japan Science and Technology Agency (JST) AIP Acceleration Research grant No. JP20317829 (AT and TN). Y.E. is also supported by JST, the establishment of university fellowships toward the creation of science technology innovation, grant No. JPMJFS2123. Numerical computations were carried out at Yukawa Institute Computer Facility, and Cray XC50 at Center for Computational Astrophysics, National Astronomical Observatory of Japan.

ORCID iDs

Takahiro Nishimichi <https://orcid.org/0000-0002-9664-0760>
Atsushi Taruya <https://orcid.org/0000-0002-4016-1955>

References

- Adhikari, S., Dalal, N., & Chamberlain, R. T. 2014, *JCAP*, 2014, 019
Ambikasaran, S., Foreman-Mackey, D., Greengard, L., Hogg, D. W., & O’Neil, M. 2015, *ITPAM*, 38, 252
Behroozi, P. S., Wechsler, R. H., & Wu, H.-Y. 2013, *ApJ*, 762, 109
Bertschinger, E. 1985, *ApJS*, 58, 39
Blumenthal, G. R., Faber, S. M., Primack, J. R., & Rees, M. J. 1984, *Natur*, 311, 517
Bullock, J. S., & Boylan-Kolchin, M. 2017, *ARA&A*, 55, 343
Diemer, B. 2017, *ApJS*, 231, 5
Diemer, B. 2023, *MNRAS*, 519, 3292
Diemer, B., & Kravtsov, A. V. 2014, *ApJ*, 789, 1
Einasto, J. 1965, *TrAlm*, 5, 87
Fillmore, J. A., & Goldreich, P. 1984, *ApJ*, 281, 1
Hahn, O., & Angulo, R. E. 2016, *MNRAS*, 455, 1115

- Klypin, A., Yepes, G., Gottlöber, S., Prada, F., & Heß, S. 2016, *MNRAS*, 457, 4340
- Klypin, A. A., Trujillo-Gomez, S., & Primack, J. 2011, *ApJ*, 740, 102
- Lithwick, Y., & Dalal, N. 2011, *ApJ*, 734, 100
- Ludlow, A. D., Navarro, J. F., Springel, V., et al. 2010, *MNRAS*, 406, 137
- More, S., Diemer, B., & Kravtsov, A. V. 2015, *ApJ*, 810, 36
- Navarro, J. F., Frenk, C. S., & White, S. D. M. 1996, *ApJ*, 462, 563
- Navarro, J. F., Frenk, C. S., & White, S. D. M. 1997, *ApJ*, 490, 493
- Navarro, J. F., Ludlow, A., Springel, V., et al. 2010, *MNRAS*, 402, 21
- Nusser, A. 2001, *MNRAS*, 325, 1397
- Peebles, P. J. E. 1982, *ApJL*, 263, L1
- Peebles, P. J. E. 1984, *ApJ*, 277, 470
- Planck Collaboration, Ade, P. A. R., Aghanim, N., et al. 2016, *A&A*, 594, A13
- Ryden, B. S. 1993, *ApJ*, 418, 4
- Sousbie, T., & Colombi, S. 2016, *JCoPh*, 321, 644
- Sugiura, H., Nishimichi, T., Rasera, Y., & Taruya, A. 2020, *MNRAS*, 493, 2765
- Taylor, J. E., & Navarro, J. F. 2001, *ApJ*, 563, 483
- Yoshikawa, K., Yoshida, N., & Umemura, M. 2013, *ApJ*, 762, 116
- Zhao, D. H., Mo, H. J., Jing, Y. P., & Börner, G. 2003, *MNRAS*, 339, 12
- Zukin, P., & Bertschinger, E. 2010, *PhRvD*, 82, 104044
- Zwicky, F. 1933, *AcHPh*, 6, 110
- Zwicky, F. 1937, *ApJ*, 86, 217